Electronic structure and optical properties of *F* centers in α-alumina

Tathagata Biswas and Manish Jain[*]

Center for Condensed Matter Theory, Department of Physics, Indian Institute of Science, Bangalore 560012, India

We use a state-of-the-art *GW* Bethe-Salpeter equation (BSE) formalism to study electronic structure and optical properties of oxygen vacancies (*F* centers) in α-alumina. The density functional theory (DFT) + *GW* formalism has been employed to compute the charge transition levels (CTLs) for oxygen vacancies. We propose a reformulation of the DFT+GW approach to calculate these CTLs. Our new approach allows for transparent application of electrostatic corrections required in finite supercell calculations using periodic boundary conditions. We find that *F* centers in this material introduce deep donor levels, (+2/+1) at 2.4 eV, and a (+1/0) level at 3.9 eV above the valence band maximum. We also study *F*-center absorption and emission processes using constrained DFT and BSE. Our calculated absorption and emission energies are in excellent agreement with experiments and provide an unambiguous interpretation of the same.

I. INTRODUCTION

Aluminium oxide (Al$_2$O$_3$) with corundum structure (α-alumina) is one of the most used structural ceramics in the world. This material is used in a wide variety of applications including high-temperature structural ceramics, abrasives, dielectric insulators, catalysts, and optical devices [1–4]. α-alumina has not only been used in traditional fields such as cutting tools in industries, substrates for the growth of thin metal, semiconductor, and insulator films, etc., but also in exciting new applications such as strong durable optical fibers and scratch resistant screens on mobile electronics devices [3,4]. This is because of the unusual combination of mechanical, chemical, and electronic properties [2] of this material.

As is well known, all material properties can change dramatically in the presence of defects in an otherwise perfect crystal [5,6]. For instance, anionic vacancies in a crystal with one or more electrons at the defect site have been found to absorb light in the visible spectrum. They can make a wide-band-gap transparent material colored [7], and are called *F* centers or color centers. Defects in aluminium oxide have been studied extensively over the last few decades to understand their role in influencing the properties of this material [7–13]. Oxygen related point defects, especially oxygen vacancies, are known to be a common defect in oxides [14]. Thermodynamic charge transition levels (CTLs) provide useful information from an electronic or optoelectronic application point of view. CTLs not only describe whether the defect is going to act as an electronic donor or acceptor but also whether it is shallow ($\sim k_BT$ from bands edges) or lies deep inside the band gap [15]. Shallow levels can introduce carriers in the nearby band edges through thermal excitations. Deep levels have been used in the recent years for various applications, such as pinning the Fermi level in an energy region far from the band edges [16,17], as single spin centers

for quantum computing in systems like the nitrogen-vacancy (NV) center in diamond [18,19], etc.

In this paper, we use a state-of-the art *GW* Bethe-Salpeter (BSE) formalism to study electronic structure and optical properties of oxygen vacancies in α-alumina. We compute thermodynamic charge transition levels (CTLs) for oxygen vacancies using the density functional theory (DFT) + *GW* formalism. We propose an alternative approach to calculate these CTLs. This approach provides an efficient way to perform electrostatic corrections. We also study *F*-center absorption and emission processes using constrained DFT and BSE.

II. COMPUTATIONAL METHODS

We perform first-principles DFT calculations using the QUANTUM ESPRESSO package [20]. We use the generalized gradient approximation (GGA) [21] for the exchange-correlation functional. Norm-conserving pseudopotentials [22] are used to describe electron-ion interactions. The electronic wave functions are expanded in plane waves with energy up to 75 Ry. The calculations for perfect crystals have been done using a unit cell containing 30 atoms and a $4 \times 4 \times 2$ k-point sampling of the Brillouin zone. For the calculations with oxygen vacancies in various charge states, we use $2 \times 2 \times 1$ and $3 \times 3 \times 1$ supercells, containing 120 and 270 atoms respectively. These supercell sizes are large enough to exclude any short-range defect-defect interactions. The Brillouin zone for $2 \times 2 \times 1$ and $3 \times 3 \times 1$ supercells is sampled using $2 \times 2 \times 2$ k-point grid and Γ point respectively. We simulate different charge states ($q = 0, 1, 2$) of the oxygen vacancy.

Quasiparticle and optical properties are calculated within the *GW*-BSE formalism as implemented in the BERKELEYGW package [23]. To compute the quasiparticle energies (E^{QP}) we solve the Dyson equation [24], where the self-energy operator [$\Sigma(E)$] has been calculated within the G_0W_0 approximation. The dielectric matrix is calculated within the random phase

---
[*]mjain@iisc.ac.in

approximation (RPA) and expressed in a plane-wave basis with plane-wave energies up to 25 Ry. The matrix is calculated at zero frequency and extended to finite frequencies using the generalized plasmon pole model proposed by Hybertsen and Louie [25]. In the case of unit cell calculations we include 1000 bands while performing the sum over unoccupied states involved in the dielectric matrix and self-energy calculations. To ensure the convergence of our results with the number of bands, we added a static remainder [26] term to the self-energy. For $2 \times 2 \times 1$ and $3 \times 3 \times 1$ supercells, we increase the number of bands to 4000 and 9000 respectively. To study electron-hole interactions and excitonic effects we solve the Bethe-Salpeter equation [27]. The electron-hole interaction kernel for BSE calculations performed on unit cells is computed with 44 valence and 11 conduction bands. The calculated kernel is extrapolated from a $4 \times 4 \times 2$ k-point grid to a $10 \times 10 \times 5$ k-point sampling of the Brillouin zone. These parameters are sufficient to obtain a converged optical spectrum for energies up to $\sim$5 eV from the absorption edge.

The formation energy of a point defect, $E_q^f(\mathbf{R})[\epsilon_F]$, in charge state q, with all the atoms at coordinates $\{\mathbf{R}\}$ and the chemical potential of the electron (Fermi level) ϵ_F, can be defined as [15]

$$E_q^f(\mathbf{R})[\epsilon_F] = E_q^{\text{def}}(\mathbf{R}) - \left[E^{\text{perf}} + \sum_i n_i \mu_i \right] + [\epsilon_F + E_v]q, \tag{1}$$

where $E_q^{\text{def}}(\mathbf{R})$ is the total energy of the defect supercell in charge state q with all the atoms at coordinates $\{\mathbf{R}\}$, and E^{perf} is the total energy of the perfect supercell (without any defects). n_i refers to the number of atoms removed ($n_i < 0$) from or added to ($n_i > 0$) the perfect supercell to make the defect supercell. The removed/added atoms are exchanged from a bath with chemical potential μ_i. It should be noted that we have defined ϵ_F with respect to valence band maxima (E_v).

Thermodynamic charge transition level (CTL), $\epsilon^{q/q-1}$, is defined as the value of the electron chemical potential (ϵ_F) at which the charge state of the defect changes from q to $q-1$. It can be written in terms of formation energies as [15]

$$\epsilon^{q/q-1} = E_{q-1}^f(\mathbf{R}_{q-1})[\epsilon_F = 0] - E_q^f(\mathbf{R}_q)[\epsilon_F = 0], \tag{2}$$

where $\{\mathbf{R}_q\}$ and $\{\mathbf{R}_{q-1}\}$ denote the equilibrium structures with defect in charge states q and $q-1$ respectively.

Within standard DFT, one can obtain the formation energies in equilibrium configurations of respective charge states and thus calculate $\epsilon^{q/q-1}$. However, as calculating CTLs involves addition or removal of one or multiple electrons, Using just the DFT formalism is expected to pose problems. To overcome this issue we have used the DFT + GW formalism [28–30]. In this method we write the CTL as

$$\epsilon^{q/q-1} = \left[E_{q-1}^f(\mathbf{R}_{q-1}) - E_{q-1}^f(\mathbf{R}_q) \right] + \left[E_{q-1}^f(\mathbf{R}_q) - E_q^f(\mathbf{R}_q) \right]$$

$$\equiv E_{q-1}^{\text{relax}}[\mathbf{R}_q] + E^{\text{QP}}(\mathbf{R}_q) \tag{3}$$

The first term ($E_{q-1}^{\text{relax}}[\mathbf{R}_q]$) on the right-hand side of Eq. (3) is a relaxation energy. For a system containing a defect in charge state $q-1$, $E_{q-1}^{\text{relax}}[\mathbf{R}_q]$ is the total energy difference

between a structure with all the atoms at coordinates $\{\mathbf{R}_q\}$ and the equilibrium structure (in this case $\{\mathbf{R}_{q-1}\}$). The relaxation energy can be computed accurately within DFT. The second term on the right-hand side of Eq. (3), $E^{\text{QP}}(\mathbf{R}_q)$, involves a change in the electron number as the defect charge changes from q to $q-1$. This is the electron affinity (EA) of a system containing a defect in charge state q with all the atoms at $\{\mathbf{R}_q\}$. This quasiparticle energy can be computed accurately using the GW formalism. Alternatively, we can write

$$\epsilon^{q/q-1} = \left[E_{q-1}^f(\mathbf{R}_{q-1}) - E_q^f(\mathbf{R}_{q-1}) \right] + \left[E_q^f(\mathbf{R}_{q-1}) - E_q^f(\mathbf{R}_q) \right]$$

$$\equiv E^{\text{QP}}(\mathbf{R}_{q-1}) - E_q^{\text{relax}}[\mathbf{R}_{q-1}] \tag{4}$$

where $E_q^{\text{relax}}[\mathbf{R}_{q-1}]$ is defined in the same way as $E_{q-1}^{\text{relax}}[\mathbf{R}_q]$ in Eq. (3) and $E^{\text{QP}}(\mathbf{R}_{q-1})$ is the ionization potential (IP) of a system containing a defect in charge state $q-1$ with all the atoms at $\{\mathbf{R}_{q-1}\}$. In Fig 1(a) we show two paths that can take the system from being at equilibrium with a defect at charge state q to one where it is at equilibrium with charge state $q-1$. Using Eq. (3) or (4) to compute $\epsilon^{q/q-1}$ is equivalent to taking the red or the blue path shown in Fig. 1(a). Following either of the two paths, one should get the same thermodynamic CTLs. This DFT + GW formalism should eliminate the errors in calculating CTLs within standard DFT.

First-principles calculations on defects often use a periodic boundary condition (PBC) with a finite supercell size. While the supercell can be made to be large enough to eliminate any short-range interaction between a defect and its periodic image, the long-range interactions, such as Coulomb interaction between charged defects, cannot be eliminated entirely. To tackle this issue, we break down the defect-defect interaction within the PBC into a short-range part such as quantum-mechanical interaction (overlap of the wave functions) and a long-range part such as elastic or electrostatic interaction. In practice, we work with a supercell size that is large enough to eliminate any short-range defect-defect interactions. For the long-range electrostatic and elastic interactions we use a correction/extrapolation scheme. As elastic interactions decay faster ($1/L^3$) than electrostatic interactions ($1/L$), typically one worries more about the latter. In this study, we use the Freysoldt—-Neugebauer—-Van de Walle (FNV) electrostatic correction scheme [31] as implemented in the CoFFEE package [32]. The single oxygen vacancy created in the supercell sizes $2 \times 2 \times 1$ (120 atoms) and $3 \times 3 \times 1$ (270 atoms) translates into defect concentrations of 8333 and 3704 ppm (parts per million) respectively. One can define the chemical formulas of the defect supercells as Al_2O_{3-x} with $x = 0.018$ and $x = 0.042$ for the 270 and 120 atom supercells respectively. By performing electrostatic correction to eliminate the effects of long-range Coulomb interaction, we study oxygen vacancies in α-alumina in the "dilute limit" [15].

While calculating relaxation energies using DFT one may be tempted to assume that the electrostatic correction involved is zero, as the total energy corrections for two formation energies with defects in the same charge state cancel each other. This is not true, as the lattice screenings in the two cases are different. The lattice relaxations in the two structures are as if they are screening different defect charges (as
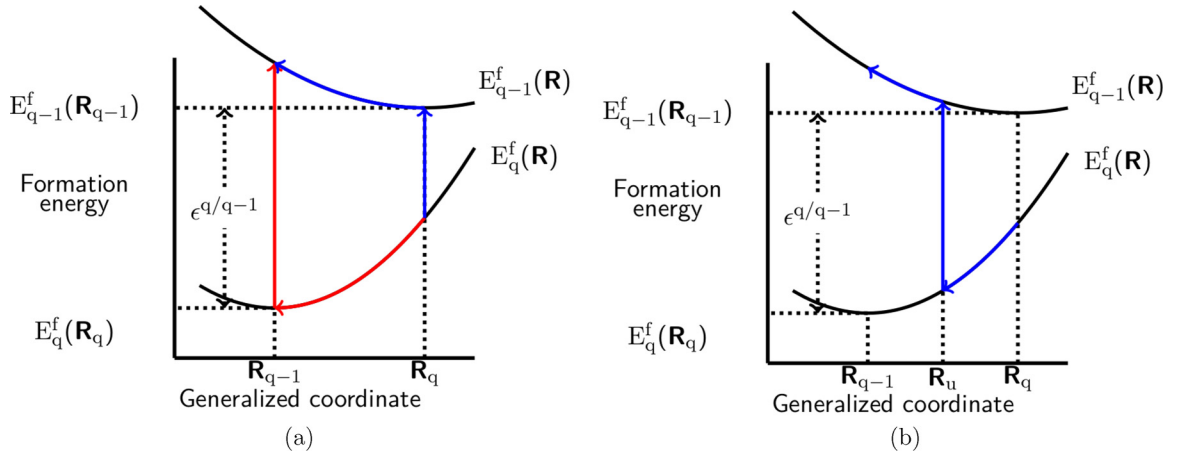
FIG. 1. Paths that can take a system at equilibrium with a defect at charge state q to one where it is at charge state $q-1$. Paths that are equivalent to using (a) Eq. (3) (red), Eq. (4) (blue), and (b) Eq. (5) are shown.

they correspond to $\{\mathbf{R}_q\}$ and $\{\mathbf{R}_{q-1}\}$). Moreover, the choice of dielectric constant, while performing eigenvalue correction to compute quasiparticle excitation energies for charged defects, is ambiguous if one uses Eq. (3) or (4). This is because an unknown fraction of lattice dielectric constant is included, owing to small supercell sizes. Using either the electronic dielectric constant (ϵ_{elec}) or the full dielectric constant (ϵ_{total}) is not expected to provide accurate electrostatic corrections.

We propose an alternative path to calculate CTLs which does not suffer from the above-mentioned issues. The CTL can be calculated using the path shown in Fig. 1(b). The CTL using this path can be written as

$$
\begin{aligned}
\epsilon^{q/q-1} &= \left[E_{q-1}^f(\mathbf{R}_{q-1}) - E_{q-1}^f(\mathbf{R}_u) \right] \\
&\quad + \left[E_{q-1}^f(\mathbf{R}_u) - E_q^f(\mathbf{R}_u) \right] + \left[E_q^f(\mathbf{R}_u) - E_q^f(\mathbf{R}_q) \right] \\
&= E_{q-1}^{\text{relax}}[\mathbf{R}_u] + E_u^{QP} - E_q^{\text{relax}}[\mathbf{R}_u],
\end{aligned}
\tag{5}
$$

where $\{\mathbf{R}_u\}$ denotes the unrelaxed structure, which can be obtained by removing an atom from a perfect supercell without changing positions of any other atoms. We compute $E_q^{\text{relax}}[\mathbf{R}_u]$ ($E_{q-1}^{\text{relax}}[\mathbf{R}_u]$) using DFT. These relaxation energies correspond to the relaxation of a defect supercell with the charge state q or $q-1$ from $\{\mathbf{R}_u\}$ to corresponding equilibrium structures. Quasiparticle excitation energy in Eq. (5) (E_u^{QP}) can be computed as either IP of the unrelaxed system with defect charge state $q-1$ (P1) or EA of the same structure with defect charge state q (P2). The choice of path shown in Fig. 1(b) is motivated by the fact that the dielectric constant required for electrostatic correction of the E_u^{QP} term is well defined (ϵ_{elec}).

To understand optical properties of the F center we relax the structure for the triplet excited state of the F center using constrained DFT. We perform a spin polarized DFT calculation and fix the occupations in such a way that one electron from a defect state gets promoted to the conduction band with its spin flipped. This occupation scheme keeps the system neutral and mimics a triplet excited state. We find that the geometries obtained within such a relaxation are very close to the F^+ geometry.

III. RESULTS AND DISCUSSION

α-alumina, which has the chemical formula Al_2O_3, consists of hexagonal unit cells (space group $R\bar{3}C$) containing 30 atoms or 6 formula units. It can also be constructed with a smaller rhombohedral unit cell containing 10 atoms (2 formula units). We have used a hexagonal unit cell of α-alumina in all our calculations.

The lattice parameters of α-alumina that we find from our calculations are in very good agreement with previous DFT calculations [9,12] and experimental values [33], as shown in Table I. Our calculations show that the band gap of this material has a strong lattice parameter dependence. We study the band gap of α-alumina as we change the in-plane lattice parameter (a) by keeping the c/a ratio fixed, using both LDA (PZ) and GGA (PBE). The results are shown in Fig. 2. The band gap of this material increases almost linearly as we decrease the in-plane lattice parameter (a). Due to the overbinding effect of LDA, the band gap of the equilibrium structure within LDA is larger compared to that found within GGA (using its equilibrium structure). As we can see in Fig. 2, the difference between GGA and LDA band gaps at their respective equilibrium lattice parameters is ∼1 eV. This difference is almost entirely because of the difference in the lattice parameters. Our results explain the large variation in the reported band gaps in the literature [9–12]. Figure 2 also shows our calculation of the GW quasiparticle gap starting from a DFT calculation with GGA at two different lattice parameter values. The GW gap also varies significantly as a function of in-plane lattice parameter, inheriting the dependence from the DFT starting point.

TABLE I. Comparison between lattice parameters and band gap values from our calculations with literature

Parameter	This work (LDA)	This work (GGA)	Ref. [12] (LDA)	Ref. [9] (GGA)	Expt. [33]
a (Å)	4.68	4.81	4.69	4.82	4.76
c (Å)	12.45	13.13	12.79	13.16	12.99
E_g (eV)	6.75	5.82	6.72	5.82	9.4
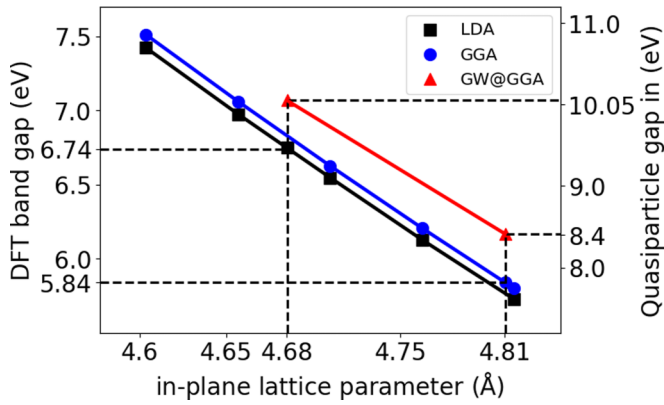
FIG. 2. Variation of band gap with lattice parameter, calculated using both GGA (blue circle) and LDA (black squares), the equilibrium lattice parameter in both cases and the corresponding band gap have been marked. In these calculations the c/a ratio was fixed to the equilibrium value. GW quasiparticle gaps starting from a DFT calculation with GGA at two different lattice parameter values have been marked with red triangles.

FIG. 3. Defect level positions and their occupations for different charge states from DFT as well as GW calculations.

Table II shows the quasiparticle band gap (E_g) and exciton binding energy (E_{EBE}) obtained from our calculations and compares them with values reported in the literature. Our calculated quasiparticle band gap is in reasonable agreement with previous GW calculations done on this material by Marinopoulos *et al.* [12]. The difference in the quasiparticle gap between two calculations can be attributed to the difference in the lattice parameters used. Marinopoulos *et. al.* [12] used lattice parameters obtained from a DFT calculation using LDA, which is expected to result in a slightly larger DFT as well as quasiparticle gap compared to one obtained using experimental lattice parameters (Fig. 2). However, the exciton binding energy reported in the aforementioned study is very close to the one we obtain using experimental lattice parameters. This suggests a weaker lattice parameter dependence of E_{EBE} compared to E_g. We also find that the GW quasiparticle gap using experimental lattice constants (9.1 eV) is in close agreement with the experimental gap at room temperature (9.31 eV) [11]. This is due to the fact that we have used the room temperature experimental lattice parameters in our studies [33].

Figure 3 shows the defect levels inside the band gap, originating from oxygen vacancies in different charge states. We show the results obtained using DFT as well as GW. The calculations were performed on a $3 \times 3 \times 1$ supercell. The position as well occupation of these defect levels for three charge states—neutral (V_O^0), +1 (V_O^{+1}), and +2 (V_O^{+2})—are

shown in the figure. For V_O^0 we find one doubly occupied spin degenerate level inside the bulk band gap. As we remove one electron from the neutral defect, the system becomes spin polarized with only one of the spin-split defect levels occupied. Removing one more electron from the defect results in an unoccupied spin degenerate level inside the gap. Quasiparticle corrections at the GW level do not move the DFT defect levels rigidly. The energy (with respect to valence band maximum) of the occupied defect levels increases by $\sim$0.3 eV, whereas that of the unoccupied levels increases by 2.1 and 2.6 eV for V_O^{+1} and V_O^{+2} respectively. It should be noted that we have included electrostatic corrections for the defect levels shown in Fig. 3. Structurally, in case of +2 and +1 charge state the four Al atoms next to oxygen vacancy on an average relax outward by $\sim$0.23 and $\sim$0.1 Å respectively, whereas, in the neutral charge state, the Al atoms relax inward by $\sim$0.05 Å.

In Table III we show thermodynamic charge transition levels calculated using Eq. (3) (P1) and Eq. (4) (P2) with two different supercell sizes, $2 \times 2 \times 1$ and $3 \times 3 \times 1$. We report the values obtained with (ec) as well as without electrostatic corrections (we) to show the importance of electrostatic correction while calculating CTLs. We have used $\epsilon = \epsilon_{elec} = 3.1$ while performing the electrostatic corrections [34]. One

TABLE II. Quasiparticle band gap and exciton binding energy obtained from our calculation compared with values reported in literature

Results (eV)	This work	Ref. [12]	Expt. [11] at 0 K	Expt. [11] at 300 K
E_g	9.1	9.36	9.57	9.31
E_{EBE}	0.37	0.4	0.13	0.15

TABLE III. CTLs calculated with two different cell sizes using Eq. (3) (P1) and Eq. (4) (P2). We report the values obtained with (ec) and without electrostatic corrections (we) and the differences between them (Δ).

CTL	$P1^{we}$	$P2^{we}$	Δ^{we}	$P1^{ec}$	$P2^{ec}$	Δ^{ec}	Mean^{ec}
$\epsilon_{120}^{+1/0}$	4.87	3.58	1.3	3.66	3.58	0.08	3.62
$\epsilon_{270}^{+1/0}$	4.86	3.77	1.09	3.96	3.77	0.19	3.86
$\epsilon_{120}^{+2/+1}$	5.14	3.72	1.42	2.79	2.51	0.28	2.65
$\epsilon_{270}^{+2/+1}$	5.04	3.84	1.20	3.23	2.94	0.29	3.08
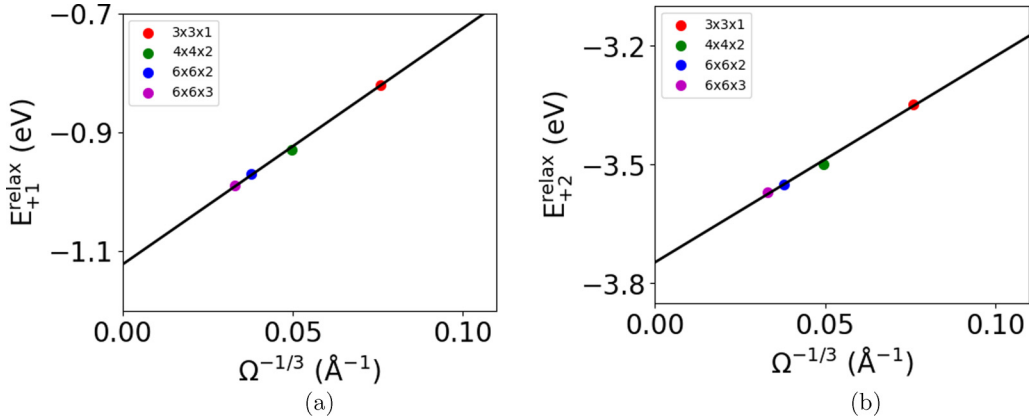
FIG. 4. Cell size dependence of the relaxation energy (E^{relax}) for defect at charge state $+1$ (a) and $+2$ (b). E^{relax} values for four different cell sizes has been used to obtain the value at infinite cell size limit ($E^{\text{relax}}[\infty]$).

can see from Table III that the CTLs calculated without electrostatic corrections following P1 and P2 are different by ~1 eV (Δ^{we}) [28]. As CTL is a thermodynamic quantity which should not depend on the path one chooses to calculate it, this discrepancy is unphysical. Once we include appropriate electrostatic corrections to E^{QP} the Δ values decrease dramatically [28]. However, it can be seen from Table III that the Δ including electrostatic corrections (Δ^{ec}) are still large and the CTLs have significant cell size dependence (Mean^{ec} for two cell sizes are significantly different). In the following sections we show that the remaining discrepancy is primarily due to the choice of dielectric constants used in electrostatic corrections. Using only the ϵ_{elec} for electrostatic corrections assumes that the charges localized at defect sites interact only though electronically screened Coulomb interaction. In this case, the lattice screening (ϵ_{latt}) does not play any role. But during the process of structural relaxation the atoms surrounding the defects move to screen the defect charges. Therefore, in any finite supercell size some lattice screening effects are automatically included. Furthermore, since we only correct the E^{QP} we assume that E^{relax} requires no electrostatic correction. In the following section we show that this assumption is not valid.

To address the above mentioned issues and to eliminate the remaining error in CTLs following P1 and P2 (Δ^{ec}) we calculate the CTLs using Eq. (5). In these calculations the quasiparticle energies have been calculated using the unrelaxed defect structures. As a result, one can justifiably use ϵ_{elec} to perform electrostatic corrections for E^{QP}. While in principle one can construct an electrostatic model for the correction to E^{relax}, we have computed it by extrapolating the relaxation energies from four supercell sizes. In Fig. 4 we show the extrapolation of E^{relax} to the infinite cell size limit using a first-order polynomial ($E^{\text{relax}}[L] = E^{\text{relax}}[\infty] + m \times L^{-1}$). We find that using higher order polynomials for the extrapolation does not significantly change the infinite cell limit of the relaxation energies ($E^{\text{relax}}[\infty]$). We use the infinite cell limit E^{relax} for the calculation of CTLs. Table IV shows the CTLs calculated using Eq. (5). The calculations have been performed for two different supercell sizes as well as two different paths. We find that the errors between the two paths (Δ) is now less than 0.2 eV. Moreover, in Table V we show

that the CTLs calculated in this way has a much smaller cell size dependence (<0.2 eV). Calculating CTL using Eq. (5) therefore provides an efficient way to perform electrostatic corrections and to obtain more accurate results than using Eq. (3) or (4). With this modified DFT + GW formalism, our calculation shows that the oxygen vacancy has two donor levels within the gap of α-alumina. It has charge transition levels ($+2/+1$) at 2.4 eV and ($+1/0$) 3.9 eV above the valence band maximum (VBM).

The lowest energy optical absorption of the F center in α-alumina involves a transition from an ^1S-like ground state to a ^1P-like singlet excited state [7,8]. The system then relaxes to a triplet excited state ^3P using a nonradiative relaxation process. The emission occurs when the system goes through a $^3P \rightarrow {}^1S$ transition. As this is a spin-forbidden transition, the lifetime of this process is very high (~36 ms) [8] and results in photoluminescence. Experimental studies of the F center in alumina [7,8] have found the absorption and emission peaks at 6.1 and 3 eV respectively.

To study F-center optical absorption we start from the neutral defect supercell. As discussed earlier, the ground state in this case has a doubly occupied defect state at 2.55 eV from the VBM (Fig. 3). To study the singlet transition ($^1S \rightarrow {}^1P$) we perform a BSE calculation including both the direct (K^d) and exchange (K^x) contributions in the electron-hole interaction kernel. We find the lowest energy exciton at 6.2 eV. This agrees very well with the experimental absorption peak at 6.1 eV [8]. Without electron-hole interaction this absorption peak would have been at 6.55 eV, indicating a considerable

TABLE IV. CTLs calculated using $2 \times 2 \times 1$ and $3 \times 3 \times 1$ supercells which contain 120 and 270 atoms respectively. We have reported values calculated using Eq. (5) with including electrostatic corrections for both E^{QP} and E^{relax}.

CTL	E_{q-1}^{relax}	E_q^{relax}	$E_{\text{P1}}^{\text{QP}}$	$\epsilon^{q/q-1}$	$E_{\text{P2}}^{\text{QP}}$	$\epsilon^{q/q-1}$	Δ
$\epsilon^{+1/0}$ (120)	−0.13	−1.12	2.91	3.90	2.87	3.87	0.03
$\epsilon^{+1/0}$ (270)	−0.13	−1.12	2.87	3.86	2.94	3.93	0.07
$\epsilon^{+2/+1}$ (120)	−1.12	−3.75	−0.19	2.44	−0.36	2.27	0.17
$\epsilon^{+2/+1}$ (270)	−1.12	−3.75	−0.14	2.49	−0.09	2.54	0.05

TABLE V. CTLs calculated using $2 \times 2 \times 1$ and $3 \times 3 \times 1$ supercells which contain 120 and 270 atoms respectively. The values reported here have been calculated using Eq. (5) including electrostatic corrections for both E^{QP} and E^{relax}.

Cell size	$2 \times 2 \times 1$ (120 atoms)	$3 \times 3 \times 1$ (270 atoms)	Δ	Mean
$\epsilon^{+1/0}$	3.88	3.89	0.01	3.88
$\epsilon^{+2/+1}$	2.35	2.51	0.16	2.43

excitonic effect with a exciton binding energy of ~ 0.35 eV. This exciton binding energy is very close to the bulk α-alumina value (0.37 eV).

We denote the singlet to triplet absorption ($^1S \rightarrow {}^3P$) and emission ($^3P \rightarrow {}^1S$) energies by E_{ab} and E_{em} respectively. From Fig. 5 which shows the energy-level scheme for absorption and emission processes of the F center in α-alumina, it is evident that E_{ab} and E_{em} are related by

$$E_{ab} = E_{em} + \left(E^{3P}[R_{1S}] - E^{3P}[R_{3P}] \right) + \left(E^{1S}[R_{3P}] - E^{1S}[R_{1S}] \right)$$

$$= E_{em} + E_{relax}^{3P} + E_{relax}^{1S}, \tag{6}$$

where E_{relax}^{3P} is the triplet excited state relaxation energy and E_{relax}^{1S} is the ground state relaxation energy. The E_{relax}^{3P} is the total energy difference (when the system is in triplet excited state) between all the atoms at the ^1S equilibrium structure ($\{\mathbf{R}_{1S}\}$) and the ^3P equilibrium structure ($\{\mathbf{R}_{3P}\}$). Similarly, E_{relax}^{1S} is the the total energy difference (when the system is in singlet ground state) between all the atoms at the ^3P equilibrium structure ($\{\mathbf{R}_{3P}\}$) and the ^1S equilibrium structure ($\{\mathbf{R}_{1S}\}$).

The emission process of the F center in α-alumina involves a $^3P \rightarrow {}^1S$ transition. To study this process we calculate the "dark" triplet solution of the BSE with the system at the equilibrium structure of the ground state. Within BSE, triplet solutions are found by making the exchange contribution (K^x) in the electron-hole kernel to be zero. We find that the lowest energy required for the triplet transition is 4.9 eV. This energy can be interpreted as E_{ab} in Eq. (6). We find the excited state relaxed geometry ($\{\mathbf{R}_{3P}\}$) using constrained DFT calculations as discussed earlier. The excited state relaxation energy (E_{relax}^{3P}) and ground state relaxation energy are then calculated using the appropriate total energies of the ($\{\mathbf{R}_{1S}\}$) and ($\{\mathbf{R}_{3P}\}$) structures. We find that E_{relax}^{3P} is 0.61 eV and E_{relax}^{1S} is 1.19 eV. Using these results in Eq. (6), we find that the emission energy is 3.1 eV. This is in excellent agreement with the experimental photoluminescence emission peak [8]. In Fig. 4 we explain the absorption and emission processes and also show all the excitation and relaxation energies calculated for F-center absorption and emission processes in α-alumina.
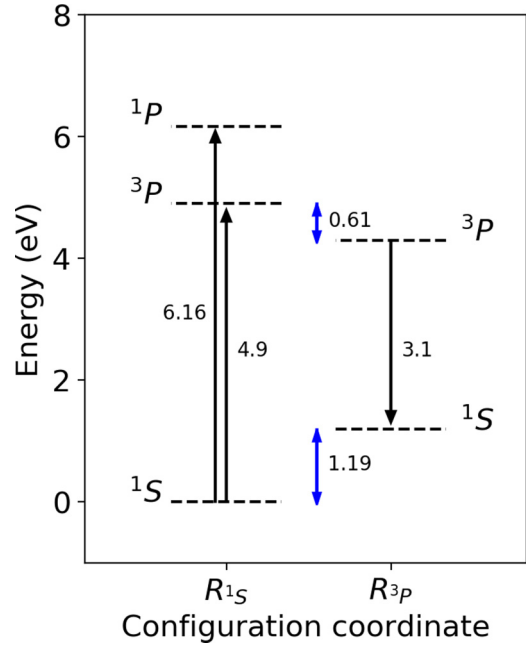
FIG. 5. Energy-level scheme for absorption and emission processes associated with the F center in α-alumina

IV. CONCLUSION

We have used first-principles methods to study electronic and optical properties of α-alumina. Using the DFT + GW formalism we calculate the thermodynamic CTLs for oxygen vacancies in this material. We propose a modified version of this formalism which can be used to perform electrostatic correction more efficiently and therefore provide more accurate CTL values. We find that oxygen vacancy in this material has deep donor levels, $(+2/+1)$ at 2.4 eV and a $(+1/0)$ level at 3.9 eV above the VBM. We also study the optical absorption and emission process of a neutral oxygen vacancy in α-alumina (F center) using GW-BSE methodology. For the photolumiscence emission process, we use constrained DFT to simulate the excited state relaxation processes. Our calculations show that the F center in α-alumina has absorption and emission peaks near 6.2 eV and 3.1 eV respectively. This is in very good agreement with previous experimental findings for this defect.

[1] M. J. Pearson, Ind. Eng. Chem. Prod. Res. Dev. **16**, 154 (1977).

[2] P. Auerkari, Tech. Res. Cent. Finl. **1792**, 26 (1996).

[3] P. Dragic, T. Hawkins, P. Foy, S. Morris, and J. Ballato, Nat. Photonics **6**, 627 (2012).

[4] J. M. Zahler and C. J. Petti, Mobile electronic device comprising an ultrathin sapphire cover plate, U.S. Patent No. 9,369,553 (2016).

[5] A. Heuer, N. J. Tighe, and R. Cannon, J. Am. Ceram. Soc. **63**, 53 (1980).

[6] R. Cannon, W. H. Rhodes, and A. Heuer, J. Am. Ceram. Soc. **63**, 46 (1980).

[7] B. D. Evans, G. J. Pogatshnik, and Y. Chen, Nucl. Instrum. Methods Phys. Res., Sect. B **91**, 258 (1994).

[8] K. H. Lee and J. H. Crawford, Jr., Phys. Rev. B **19**, 3217 (1979).

[9] K. Matsunaga, T. Tanaka, T. Yamamoto, and Y. Ikuhara, Phys. Rev. B **68**, 085110 (2003).

[10] R. H. French, J. Am. Ceram. Soc. **73**, 477 (1990).

[11] R. H. French, D. J. Jones, and S. Loughin, J. Am. Ceram. Soc. **77**, 412 (1994).

[12] A. G. Marinopoulos and M. Grüning, Phys. Rev. B **83**, 195129 (2011).

[13] M. Choi, A. Janotti, and C. G. Van de Walle, J. Appl. Phys. **113**, 044501 (2013).

[14] C. T. Campbell and C. H. Peden, Science **309**, 713 (2005).

[15] C. Freysoldt, B. Grabowski, T. Hickel, J. Neugebauer, G. Kresse, A. Janotti, and C. G. Van de Walle, Rev. Mod. Phys. **86**, 253 (2014).

[16] J. Robertson, O. Sharia, and A. Demkov, Appl. Phys. Lett. **91**, 132912 (2007).

[17] D. J. Chadi, P. H. Citrin, C. H. Park, D. L. Adler, M. A. Marcus, and H.-J. Gossmann, Phys. Rev. Lett. **79**, 4834 (1997).

[18] J. Weber, W. Koehl, J. Varley, A. Janotti, B. Buckley, C. Van de Walle, and D. D. Awschalom, Proc. Natl. Acad. Sci. USA **107**, 8513 (2010).

[19] S. K. Choi, M. Jain, and S. G. Louie, Phys. Rev. B **86**, 041202(R) (2012).

[20] P. Giannozzi, S. Baroni, N. Bonini, M. Calandra, R. Car, C. Cavazzoni, D. Ceresoli, G. L. Chiarotti, M. Cococcioni, I. Dabo *et al.*, J. Phys.: Condens. Matter **21**, 395502 (2009).

[21] J. P. Perdew, K. Burke, and M. Ernzerhof, Phys. Rev. Lett. **77**, 3865 (1996).

[22] N. Troullier and J. L. Martins, Phys. Rev. B **43**, 1993 (1991).

[23] J. Deslippe, G. Samsonidze, D. A. Strubbe, M. Jain, M. L. Cohen, and S. G. Louie, Comput. Phys. Commun. **183**, 1269 (2012).

[24] L. Hedin and S. Lundqvist, Solid State Phys. **23**, 1 (1970).

[25] M. S. Hybertsen and S. G. Louie, Phys. Rev. B **34**, 5390 (1986).

[26] J. Deslippe, G. Samsonidze, M. Jain, M. L. Cohen, and S. G. Louie, Phys. Rev. B **87**, 165124 (2013).

[27] M. Rohlfing and S. G. Louie, Phys. Rev. B **62**, 4927 (2000).

[28] M. Jain, J. R. Chelikowsky, and S. G. Louie, Phys. Rev. Lett. **107**, 216803 (2011).

[29] P. Rinke, A. Janotti, M. Scheffler, and C. G. Van de Walle, Phys. Rev. Lett. **102**, 026402 (2009).

[30] M. Hedström, A. Schindlmayr, G. Schwarz, and M. Scheffler, Phys. Rev. Lett. **97**, 226401 (2006).

[31] C. Freysoldt, J. Neugebauer, and C. G. Van de Walle, Phys. Rev. Lett. **102**, 016402 (2009).

[32] M. H. Naik and M. Jain, Comput. Phys. Commun. **226**, 114 (2018).

[33] W. Lee and K. Lagerlof, J. Electron Microsc. Technol. **2**, 247 (1985).

[34] Y. Kumagai and F. Oba, Phys. Rev. B **89**, 195205 (2014).